Effect of Planar Flow Melt Spinning Parameters on Ribbon Formation in Soft Magnetic $Fe_{68.5}Si_{18.5}B_9Nb_3Cu_1$ Alloy

M. SRINIVAS, B. MAJUMDAR, G. PHANIKUMAR, and D. AKHTAR

The effect of planar flow melt spinning (PFMS) parameters on the continuity, surface quality, and structure of 10-mm-wide $Fe_{68.5}Si_{18.5}B_9Nb_3Cu_1$ ribbons has been investigated. The change in shape and stability of the melt puddle as a function of the processing parameter was studied using a high-speed imaging system and was correlated to ribbon formation. A window of process parameters for obtaining continuous ribbons with good surface quality has been evaluated. It has been observed that thinner ribbons are found to be more continuous because of higher ductility. The higher melt temperature leads to the formation of crystalline phase in as-spun ribbons, and this deteriorates the soft magnetic properties on annealing. The experimental results are corroborated with the numerical estimates, which suggest that the critical thickness for amorphous phase formation decreases with increasing initial melt temperature.

I. INTRODUCTION

OF the rapid solidification techniques developed over the past few decades, the planar flow melt spinning (PFMS) process[1] has gained much importance commercially because of its capability of producing thin, wide, and continuous ribbons. The process is used extensively for producing Fe-based soft magnetic ribbons for transformer applications, as most of the soft magnetic materials are used in the form of ring cores or torroid, which can be fabricated directly from the ribbons.

Because the permeability and lamination factor of a transformer core depend on the structure and surface quality of the ribbons,[2] it is essential to produce wide and continuous amorphous ribbons with good surface finish. The formation of quality ribbon by the PFMS process depends on the shape and stability of the melt puddle formed between the nozzle and the rotating copper wheel.[3] A continuous ribbon is obtained only when a dynamic equilibrium is established in the puddle. Several process parameters such as nozzle wheel gap, wheel speed, initial melt temperature, ejection pressure, *etc.* and material properties such as density, surface tension, viscosity, thermal conductivity, *etc.* influence the quality and soft magnetic properties of the as-spun ribbons.

The severe conditions in the PFMS process (high wheel speed, large thermal gradients, small dimensions of the active zone, and small durations of the process) impose considerable restrictions on experimental investigations and therefore require numerical modeling to describe the real-time situation. Attempts have been made to predict numerically the thickness obtained under a given set of parameters.[4–7] Although numerical simulation of the PFMS process has been reported by several authors[8–10] to predict the fluid flow and temperature distributions in the puddle, experimental evidence of the variations in the puddle geometry with change in process parameters is limited. Few investigations using a high-speed camera have been carried out to study the transient shape of the puddle as a function of processing parameters.[4,11,12] However, these studies have been carried out on Al-based alloys using a backlight technique, and not many reports are available on puddle dimension of Fe-based alloys. Moreover, a window of processing parameters for these commercially important alloys is not available in the literature.

$Fe_{73.5}Si_{13.5}B_9Nb_3Cu_1$ alloy (FINEMET) ribbons produced by the PFMS process have attracted considerable interest as they possess a unique combination of soft magnetic properties that are superior to the conventional soft magnetic materials.[13] Detailed investigations were carried out to optimize the structure and soft magnetic properties of Fe-Si-B-Nb-Cu alloys with respect to the composition and process parameters.[14] The kinetics of nanocrystallization have also been studied for the alloys of different compositions.[15,16] The current investigators have observed that amorphous phase forms in the alloy of $Fe_{68.5}Si_{18.5}B_9Nb_3Cu_1$ composition even at a wheel speed as low as 12 m/s reveal a better glass-forming ability compared with other compositions.[17] Moreover, the alloy around this composition has near-zero magnetostriction value,[18] which should result in better soft magnetic properties.

In the current study, the effect of the PFMS process parameters on the continuity and thickness of 10-mm-wide amorphous ribbons of $Fe_{68.5}Si_{18.5}B_9Nb_3Cu_1$ alloy has been studied using a laboratory-scale melt spinner.

M. SRINIVAS, Scientist B, B. MAJUMDAR, Scientist E, and D. AKHTAR, Scientist G, are with the Advanced Magnetics Group, Defence Metallurgical Research Laboratory, Hyderabad 500 058, India. Contact e-mail: bhaskar@dmrl.drdo.in G. PHANIKUMAR, Associate Professor, is with the Department of Metallurgical & Materials Engineering, Indian Institute of Technology Madras, Chennai 600 036, India.

An attempt has been made to estimate numerically the role of melt temperature on the critical thickness for glass formation.

II. EXPERIMENTAL

An alloy of nominal composition $Fe_{68.5}Si_{18.5}B_9Nb_3Cu_1$ (at. pct) was prepared by melting the elemental mixture of pure Fe, Si, B, Nb, and Cu in a vacuum-induction melting furnace. A high-temperature differential scanning calorimeter (NETZSCH STA 409, Netzsch Instruments N.A. LLC, Burlington) was used to determine the melting point and enthalpy of fusion. Amorphous ribbons were produced using a vacuum melt spinner by remelting 30 g alloy in a quartz crucible whose bottom is in the form of a slit nozzle with rectangular cross section (10 mm × 0.5 mm) and ejecting onto a rotating Cu wheel (300 mm diameter). Because the ambient condition has practically no effect on the structure, thermal stability, and magnetic properties of these alloys,[14] all experiments were carried out in air. The following parameters were varied systematically (within the range given in bracket), one at a time keeping other parameters constant:

(a) Nozzle-wheel gap, G (0.1 to 0.5 mm)
(b) Melt temperature, T (1373 K to 1823 K [1100 °C to 1550 °C])
(c) Wheel speed, V (12 to 51 m/s)
(d) Ejection pressure, P (0.1 to 0.7 kg/cm^2)

It might be noted that the initial and final stages of the process are influenced by the transient flow conditions resulting in the formation of discontinuous and irregular ribbons. Therefore, the ribbons produced during intermediate stage have been considered for evaluation.

The formation of the puddle during melt spinning was recorded using high-speed videography (FALCON 1.4M100, Dalsa Waterloo, Ontario, Canada) at a speed of 100 frames/s and the images were analyzed using Image Pro software. Calibration of the puddle

dimensions was carried out by nozzle-wheel gap measurement as reference. The surface roughness of the as spun ribbons was measured using surf analyzer 4500. Strain to fracture (ε) of the as spun ribbons was measured by bend test using the following formula[19]:

$$\varepsilon = \frac{x}{d - x} \times 100 \qquad [1]$$

where x and d represent the thickness of the ribbon and the distance between the edges of the ribbon before fracture, respectively.

As-spun ribbons were annealed in a vacuum tubular furnace (2×10^{-5} mbar) at a temperature of 823 K (550 °C) for 1 hour. Structural characterization of the as-spun and annealed ribbons was carried out using an X-ray diffractometer (XRD) (Philips-PW1830, Philips Electronic Corp., Mahwah, NJ). Microstructural evaluation was carried out using a transmission electron microscope (TEM) (JEOL 2000FX, Japan Electron Optics Ltd., Tokyo, Japan). The precision ion polishing system was employed for TEM sample preparation by thinning from both the sides of the ribbon. The coercivity of as-spun and annealed ribbons was measured using a coercimeter (FÖSTER-KOERZIMET 1.095, Institut Dr. Foerster Gmbh & Co KG, Reutligen, Germany).

III. RESULTS

A. Puddle Geometry

Figure 1 shows high-speed images of the melt puddle formed during melt spinning at different processing conditions, keeping melt temperature constant at 1523 K to 1573 K (1250 °C to 1300 °C) in all the runs. Figure 1(a) shows the image of the puddle when V = 17 m/s, G = 0.2 mm, and P = 0.1 kg/cm^2. Figures 1(b) and (c) show the puddle shape when the ejection pressure (P) increases to 0.3 and 0.7 kg/cm^2, respectively, keeping the other parameters constant (V = 17 m/s and G = 0.2 mm). It can be observed that

(a) P= 0.1 kg/cm2, V=17 m/s, G=0.2 mm

(b) P=0.3 kg/cm2, V=17m/s, G=0.2 mm
(d) V=34m/s, P= 0.1 kg/cm2, G=0.2 mm
(f) G=0.3 mm, P= 0.1 kg/cm2, V=17 m/s

(c) P= 0.7 kg/cm2, V=17m/s, G=0.2 mm
(e) V=51m/s, P= 0.1 kg/cm2, G=0.2 mm
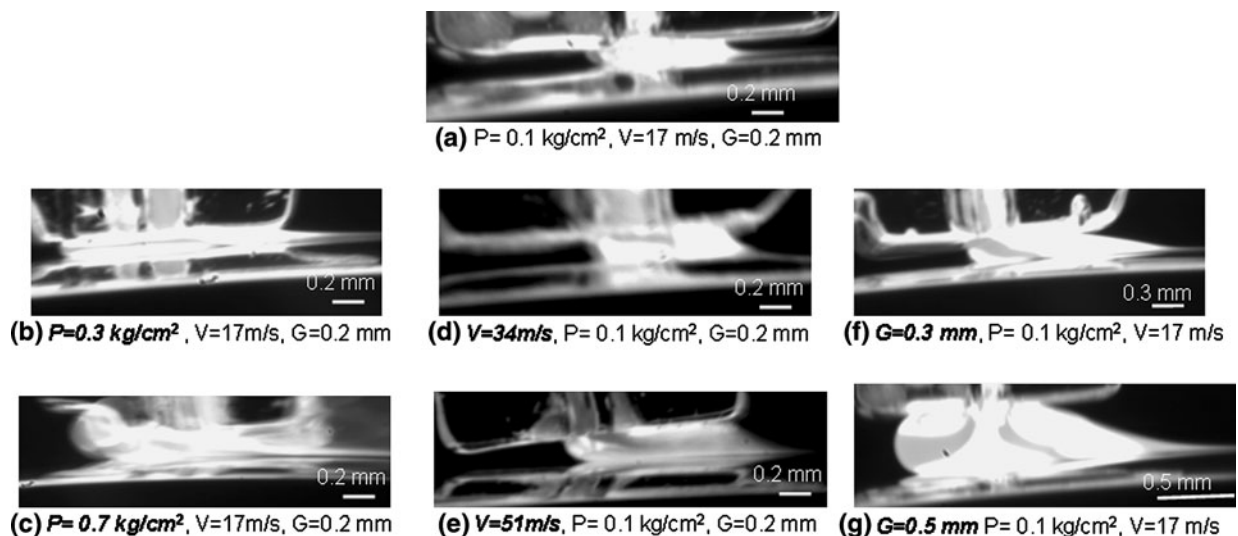(g) G=0.5 mm P= 0.1 kg/cm2, V=17 m/s

Fig. 1—High-speed images of the melt puddle at different ejection pressure, wheel speed, and nozzle wheel gap.

the puddle length increases on increasing the ejection pressure (Figure 1(b)) and a subsequent increase to 0.7 kg/cm^2 leads to the rupture of a downstream meniscus (Figure 1(c)). Figures 1(d) and (e) show the puddle shape when the wheel speed (V) changes from 17 m/s (Figure 1(a)) to 34 m/s and then to 51 m/s, respectively, keeping the other parameters constant (G = 0.2 mm and P = 0.1 kg/cm^2). The length of the puddle increases with wheel speed leading to the shift of upstream meniscus toward the right. It is to be mentioned that the fluctuation in the puddle length increases with the wheel speed. The severe oscillation of the downstream meniscus was noticed during processing at the wheel speed of 51 m/s. Figures 1(f) and (g) show the puddle shapes when the nozzle wheel gap (G) changes from 0.2 (Figure 1(a)) to 0.3 mm and then to 0.5 mm, respectively, keeping the other parameters constant (V = 17 m/s and P = 0.1 kg/cm^2). It can be observed that the flow of the melt in the puddle increases with gap. In case of the 0.5 mm gap, the contours of recirculation flow can be observed.

B. Surface Quality

Figure 2 shows the wheel side surface topography of ribbons obtained at different processing conditions keeping the nozzle wheel gap at 0.2 mm. The ribbons in Figures 2(a) through (f) were processed at different melt temperatures from 1373 K to 1809 K (1100 °C to 1536 °C) keeping the wheel speed at 34 m/s, whereas ribbons in Figures 2(g) and (h) were processed at 17 m/s and 12 m/s, keeping the melt temperature at 1573 K (1300 °C). In case of processing at 34 m/s wheel speed, the ribbons exhibit protruded striations with nonuniform,

serrated edges when the melt temperature was 1373 K to 1473 K (1100 °C to 1200 °C). The surface becomes smooth at the melt temperature of 1523 K to 1573 K (1250 °C to 1300 °C). The striations turn into grooves and then porosity along the ribbon length with nonuniform edges as the melt temperature increases above 1673 K (1400 °C). It is interesting to note that the ribbon surface changes from striated to wavy at 17 m/s and to smooth surface at a lower wheel speed of 12 m/s (Figures 2(g) and (h)). Figure 3 shows the variation of the mean surface roughness value with melt temperature (Figure 3(a)) and wheel speed (Figure 3(b)). It can be observed that the surface roughness increases with wheel speed. The roughness decreases initially with melt temperature, attains a minima in the range of 1473 K to 1573 K (1200 °C to 1300 °C), and then increases again.

C. Ribbon Dimensions

Although discontinuity in ribbon length exists for all experiments, the longest continuous ribbon obtained for a particular experimental run has been considered as the length of a ribbon. Figure 4 shows the continuous ribbon length obtained and the ribbon thickness with ejection pressure, keeping other parameters constant (nozzle wheel gap at 0.2 mm, wheel speed at 17 m/s, and melt temperature in the range of 1523 K to 1573 K [1250 °C to 1300 °C]). It can be observed that the maximum length of the continuous ribbon decreases and its thickness increases with ejection pressure. Figure 5 shows the variation of the maximum ribbon length and ribbon thickness with wheel speed keeping the nozzle wheel gap at 0.2 mm and the melt temperature in the
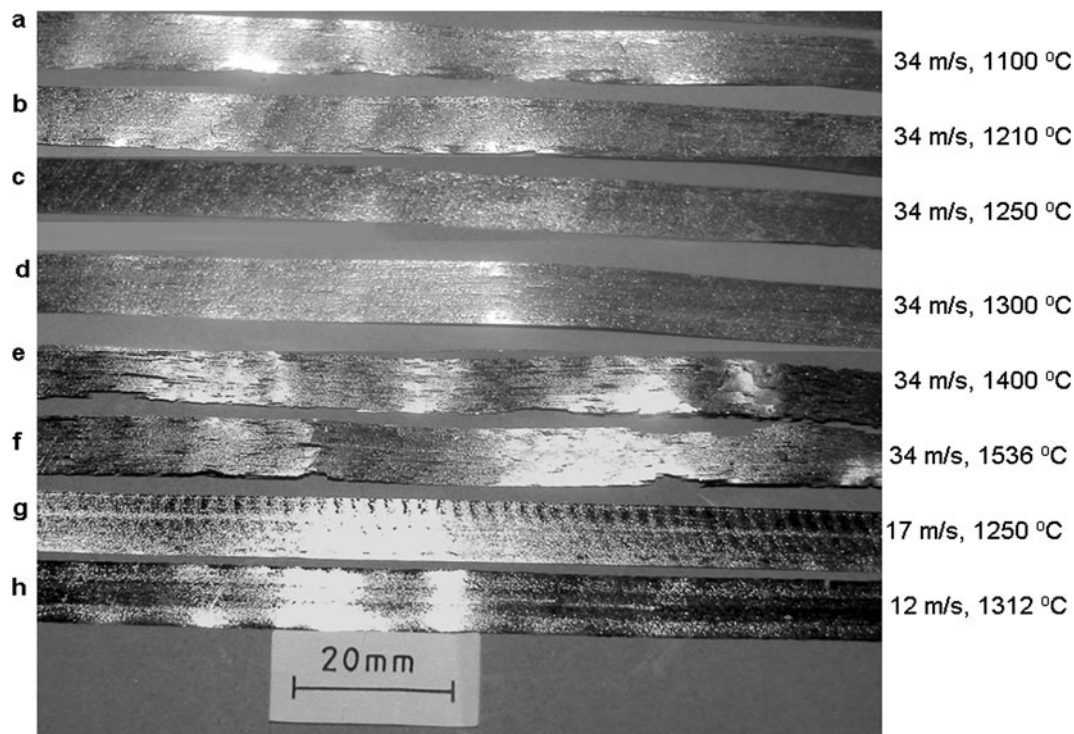

Fig. 2—Surface topography of the PFMS ribbons at different processing conditions.
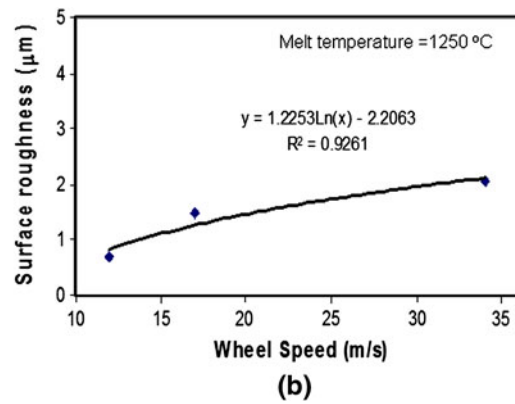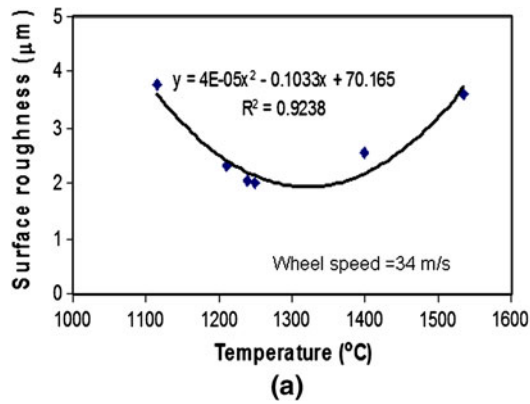
Fig. 3—Variation of surface roughness with (*a*) initial melt temperature and (*b*) wheel speed.
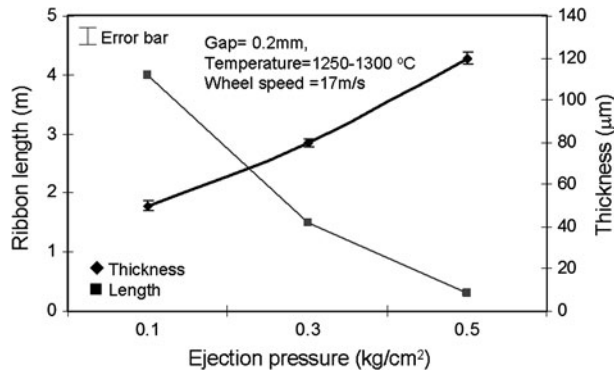

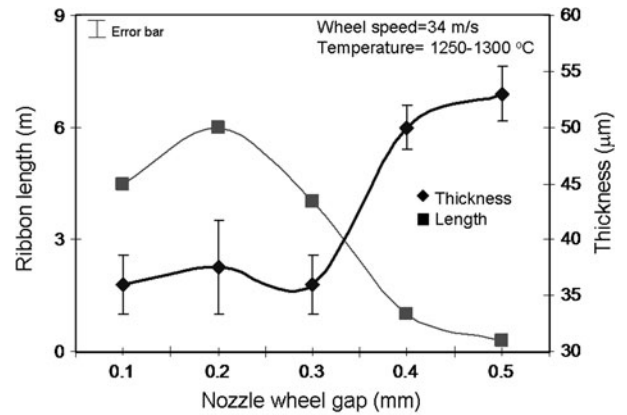Fig. 4—Variation of the length and thickness of the ribbon with ejection pressure.

Fig. 6—Variation of the length and thickness of the ribbon with nozzle wheel gap.
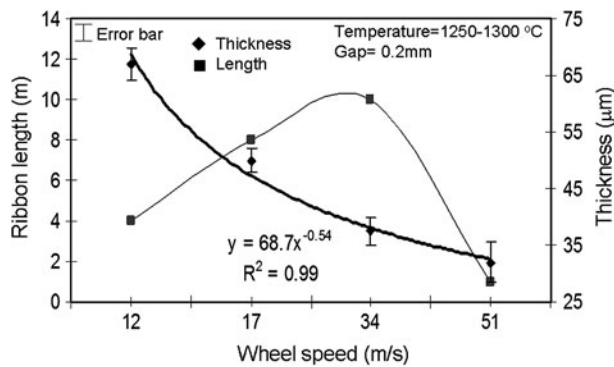

Fig. 5—Variation of the length and thickness of the ribbon with wheel speed.
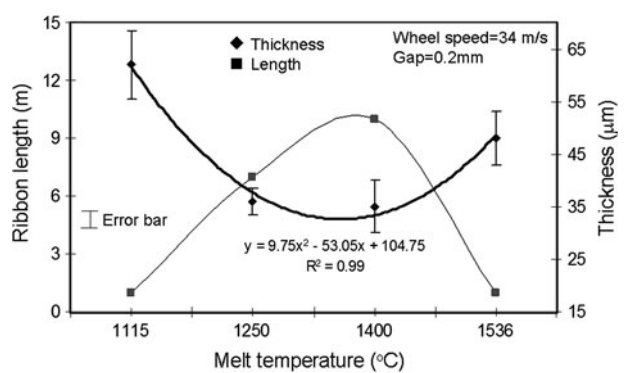

Fig. 7—Variation of the length and thickness of the ribbon with melt temperature.

range of 1523 K to 1573 K (1250 °C to 1300 °C). It can be observed that the maximum length of the continuous ribbon increases with wheel speed up to 34 m/s and then decreases at higher wheel speed. The thickness is found to decrease continuously with wheel speed. A regression analysis revealed that the thickness varies inversely with the wheel speed to the power of –0.54, which is in agreement with the reported values.[20]

Figure 6 shows the variation of maximum length and thickness of the continuous ribbon with the nozzle-wheel

gap when the wheel speed is kept constant at 34 m/s and melt temperature is kept in the range of 1523 K to 1573 K (1250 °C to 1300 °C). It can be observed that maximum length increases when the gap is enhanced to 0.2 mm and then decreases with the gap. The ribbon thickness shows a sigmoidal behavior with the gap; *i.e.*, initially, it remains almost unaltered up to 0.3 mm gap and increases rapidly at higher gaps. Figure 7 shows the maximum length and thickness of the ribbon as a function of melt temperature keeping the nozzle wheel
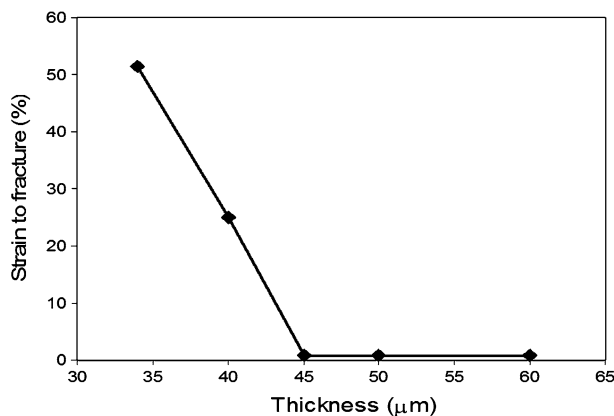
Fig. 8—Strain to fracture of the melt spun ribbons *vs* ribbon thickness.

Fig. 9—XRD patterns of the ribbons processed at different initial melt temperature of (*a*) 1523 K (1250 °C) (*b*) 1809 K (1536 °C).

gap at 0.2 mm and wheel velocity at 34 m/s. Both sets of data were best fitted with second-order polynomial curves. It can be observed that the maximum length with the melt temperature attains a maximum and then decreases, whereas the thickness of the ribbon decreases, attains a minimum, and then increases with the melt temperature. Similar observations have been reported in the literature.[7] The initial decrease in thickness might be attributed to the decrease in surface tension of the melt, which causes spreading of liquid on the wheel. The increase in thickness at higher superheat temperature might be related to the decrease in viscosity of the melt, causing a higher melt flow rate.

Figure 8 shows the strain to fracture (*ε*) of the as-spun ribbons measured by bend test as a function of thickness. It is evident that the strain before fracture decreases with increasing thickness and the ribbon becomes completely brittle beyond 45-*μ*m thickness, although it is still amorphous. This finding suggests that thinner ribbons are likely to be more continuous compared with thicker ones.

D. *Structure and Properties*

Figure 9 shows XRD patterns of the as-spun ribbons produced at a wheel speed of 17 m/s from different initial melt temperatures of 1523 K and 1809 K (1250 °C and 1536 °C). A diffuse intensity maxima in XRD pattern observed in Figure 9(a) corresponds to the presence of a fully amorphous phase, whereas in Figure 9(b) (ribbon processed at a temperature of 1809 K [1536 °C]), crystalline peaks of Fe_3Si phase are found superimposed on the diffuse intensity. Figure 10(a) shows the bright-field TEM image of the as-spun ribbon processed at a melt temperature of 1523 K (1250 °C). The featureless contrast and the broad halo ring in the selected-area diffraction (SAD) pattern indicate the presence of complete amorphous phase in as spun condition. On annealing, the nanocrystalline Fe_3Si phase precipitates in the amorphous matrix (Figure 10(b)). Figure 10(c) shows the bright-field TEM image of the ribbon spun from a melt temperature of 1809 K (1536 °C), which indicates the presence of Fe_3Si phase (dendrite) in the amorphous matrix. Annealing of these ribbon leads to
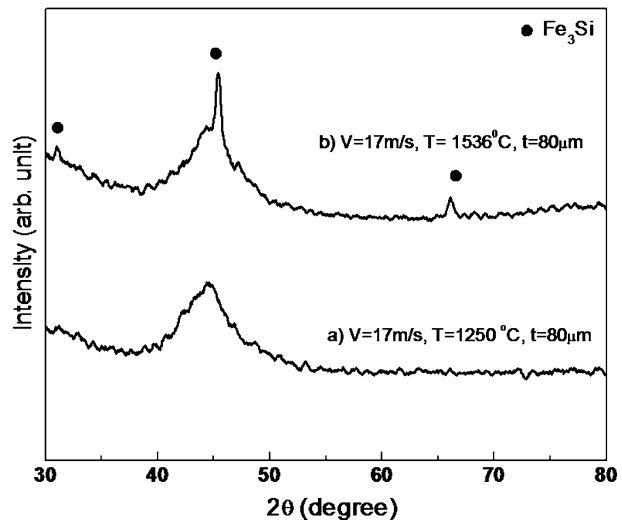
the precipitation of nanocrystalline phase from the amorphous matrix (Figure 10(d)). It can be observed that the density of the nanocrystalline phase has increased drastically compared with the Figure 10(b).

It is to be noted, on the one hand, that the coercivity of the as-spun ribbon with a completely amorphous phase (Figure 10(a)) is 0.12 Oe, which decreases on annealing by an order of magnitude to 0.028 Oe (Figure 10(b)). On the other hand, the coercivity of the ribbon with initial Fe_3Si dendrites (Figure 10(c)) is 0.24 Oe, which increases to 0.48 Oe on annealing (Figure 10(d)).

IV. DISCUSSION

A. *Ribbon Characteristics*

Assuming that a stable puddle leads to the formation of lengthy ribbon, one can expect from Figure 1(a) that lower values of pressure, nozzle wheel gap, and wheel speed can result in obtaining longer ribbons. From Figures 4 through 6, it is evident that lengthy ribbons have been obtained at a pressure of 0.1 kg/cm², an intermediate gap of 0.2 mm, and a wheel speed of 34 m/s. It is interesting to note that lengthy ribbons were obtained when the ribbon was also thin. An exception is the case of 51 m/s, in which severe oscillations in the downstream meniscus of the puddle resulted in obtaining discontinuous ribbons even though the thickness is low. Strain measurements of the as-spun ribbons in Figure 8 show that thicker ribbons fracture at a lower strain. Barth *et al.*[21] reported that the ductile-to-brittle transition temperature (DBTT) of the amorphous Fe-Si-B ribbon produced by a melt spinning route increases with the thickness because of the change of viscosity during solidification. Their results indicated that the DBTT of 40-*μ*m thick ribbon is close to room
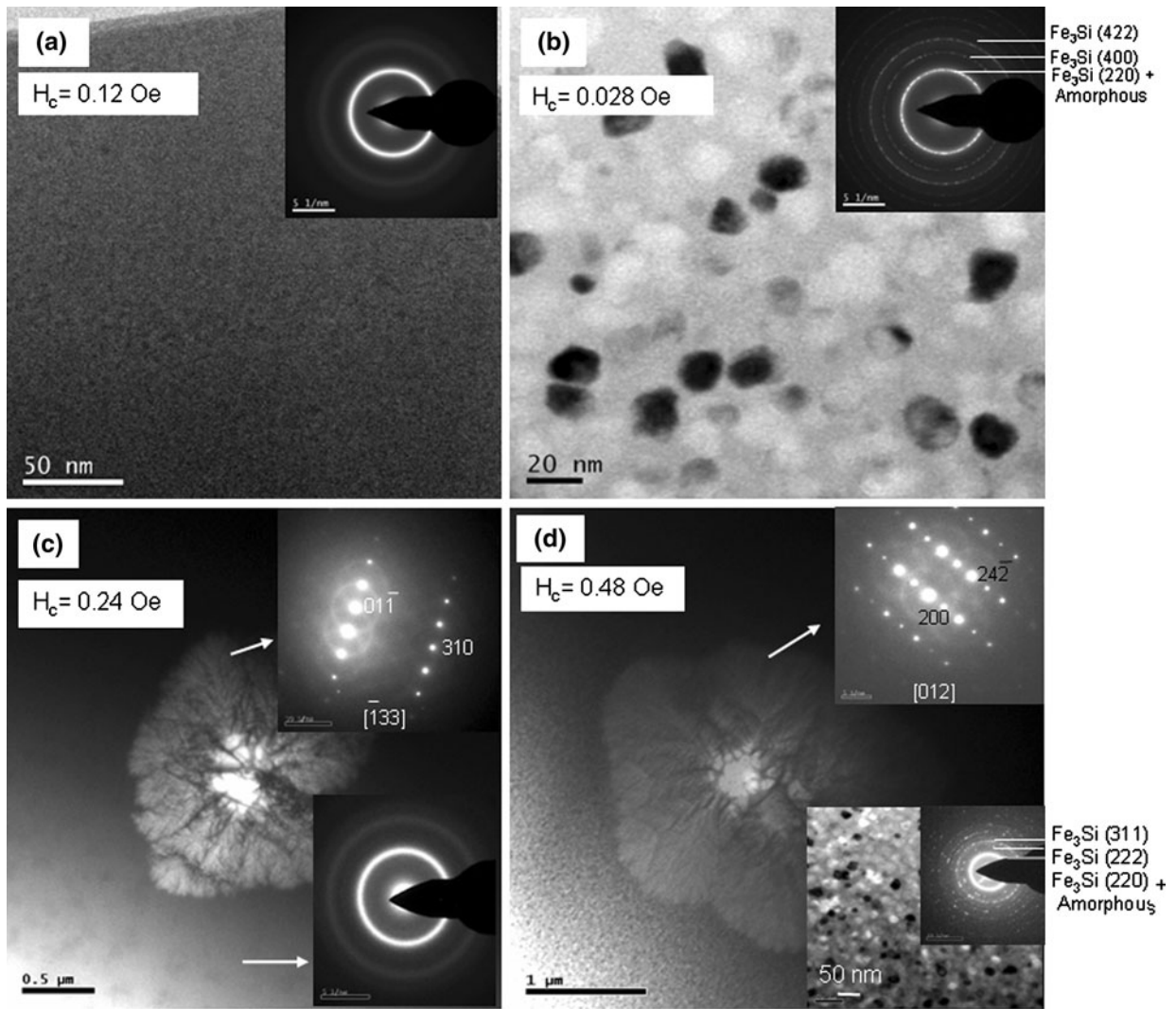
Fig. 10—TEM image and SAD patterns of (*a*) as-spun, (*b*) annealed ribbons produced at initial melt temperature of 1523 K (1250 °C) and (*c*) as-spun, (*d*) annealed ribbons produced at initial melt temperature of 1809 K (1536 °C). Inset in (*d*) enlarged portion of the nanocrystals.

temperature. Amorphous ribbons of $Fe_{68.5}Si_{18.5}B_9Nb_3Cu_1$ alloy are found to be brittle at room temperature beyond 45-μm thickness in agreement with the preceding observation.

It is evident that either protruded striation at lower temperature or grooves/porosity along the ribbon length at higher temperature (Figure 2) are responsible for higher roughness values (Figure 3(a)). Moreover, wheel speed increases the roughness (Figure 3(b)). Similar observations on surface quality have been reported previously by various authors. Carpenter and Steen[22] observed a dimple, streak, or herringbone pattern and attributed their findings to the instability caused by the Marangoni flow of liquid in the puddle. Praisner *et al.*[7] reported that a high-quality ribbon was produced at an intermediate super heat temperature, which is in agreement with the current observation. Although any conclusive explanation is not available, it is suggested that stability of the fluid flow in the puddle controls the surface morphology of the ribbon.[22] Any fluctuation or instability on the liquid surface results in the formation

of ripple and ultimately gets frozen into the ribbon. Following Rayleigh on the instability of the fluid, the solution of the time-dependent perturbation function incorporating the Gibbs-Thompson relation on pressure difference associated with the rate of change of amplitude ($\dot{\varepsilon} = \delta\varepsilon/\delta t$) is given by the following[23]:

$$\frac{\dot{\varepsilon}}{\varepsilon} = \frac{D_s \sigma \gamma \Omega^2}{kT} \left(\frac{2\pi}{\lambda_r}\right)^2 \left\{ \left(\frac{1}{r}\right)^2 - \left(\frac{2\pi}{\lambda_r}\right)^2 \right\} \quad [2]$$

where ε and λ_r are the amplitude and wavelength of perturbation at time t, r is the thickness of the liquid pool, D_s denotes the diffusion coefficient, σ is the surface tension, γ is the number of atoms per unit surface area that can diffuse, and Ω is the molar volume of the liquid in the molten pool. It is evident from the Eq. [2] that the reduction of amplitude enhances the stability of perturbation, which is directly proportion to $D_s\sigma/T$. Both D_s and σ are related to temperature (T) as:

$$D_s = D_0 e^{-\frac{E}{RT}} \quad [3]$$

and

$$\sigma = C(T_c - T) \qquad [4]$$

where D_0 is the diffusion constant, E is the activation energy for diffusion, T_c is the critical temperature of the liquid, C is constant, and R is the universal gas constant. From the preceding expressions, it can be observed that D_s increases exponentially with $-1/T$, whereas σ reduces linearly with temperature. This finding implies that the effect of diffusion is pronounced at low temperatures, and one can expect that the stability of the liquid initially with temperature increases because of the increase of diffusion resulting in the formation of a smooth ribbon surface. At higher temperatures, the surface tension effect is more pronounced and increases the instability resulting in the formation of grooves in the ribbon. Air entrapment at higher temperatures can cause porosity and increase roughness.

From Eq. [2], it is evident that perturbation increases with decreasing the thickness (r) of the liquid in the puddle. As the puddle controls the thickness of the ribbon, which is inversely proportional to the wheel speed (Figure 5), it can be inferred that the roughness will increase with the wheel speed. This finding is in agreement with the current observations.

B. Window of Process Parameters

The combined effect of all the process parameters for a successful run (continuous ribbon without defects) can be visualized by mapping the processing window in PG/2σ (maximum operating value of pressure parameter) *vs* Reynolds number (Re) diagram.[7] The values of temperature-dependent viscosity (η) and surface tension (σ) have been taken from the measured values of the similar systems given by Chen Dong *et al.*[24] and Tomut and Chiriac,[25] respectively. Figure 11 shows the processing map for successful (continuous ribbon without defects having minimum length of 1 m and same width as nozzle slit length) and unsuccessful runs (ribbons having either porosity, width less than desired, or length less than 1 m). It is interesting to note that the experiments

Fig. 11—Processing window for PFMS experiments.

are successful at lower Re and PG/2σ values. This is in conformity with the results reported for Pb-Sn system.[7] Failure experiments above a critical value of PG/2σ indicate the high-pressure boundary (blow out pressure of the meniscus) as observed by Carpenter and Steen.[22] It is noteworthy that although the Re numbers are high, the mass suction effect stabilizes the flow and maintains a laminar flow.[3]

C. Critical Thickness for Amorphous Phase

Both XRD and TEM analyses of the as-spun and annealed ribbons indicate that the initial melt temperature affects the glass formation and thereby phase evolution, which alters the soft magnetic properties after annealing. It is well known that low coercivity of nanostructured Fe-Si-B-Nb-Cu alloy arises because of the diminishing value of average magnetocrystalline anisotropy ($\langle K \rangle$) and saturation magnetostriction (λ) only when the grain size is less than the exchange interaction length of approximately 20 nm.[26] Our results indicate that the fully amorphous and annealed ribbon shows very low coercivity where as the coercivity of partially crystalline and annealed ribbons is higher because of the formation of micron- sized Fe_3Si phase, which increases the $\langle K \rangle$ value.
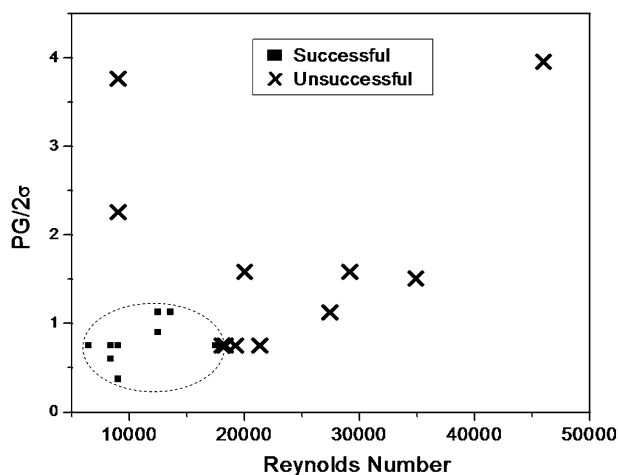
To understand the phenomena as to how the initial melt temperature affects the glass formation, detailed calculations have been carried out to predict the critical thickness for the formation of amorphous phase when the alloy is allowed to solidify from different melt temperatures. The critical thickness for the formation of amorphous phase in $Fe_{68.5}Si_{18.5}B_9Nb_3Cu_1$ alloy has been determined by superimposing the cooling curves calculated at the surface of ribbons of different thicknesses on the TTT curve for homogeneous nucleation. When the cooling curve for a given ribbon thickness touches the nose of the TTT curve, the corresponding thickness can be termed as the critical thickness for the formation of amorphous phase.

The cooling curves of ribbons at different thickness and pouring temperature were determined by solving the one-dimensional (1-D) heat flow equation using explicit finite difference method.[27] The 1-D heat flow equation is given as

$$\frac{1}{\alpha}\frac{\partial T}{\partial t} = \frac{\partial^2 T}{\partial x^2} \qquad [5]$$

where T is temperature at time t at a distance x from the wheel side surface along the ribbon thickness. α is the thermal diffusivity and equals to $k/\rho C_p$. Figure 12 shows the schematic of the melt spinning process where the ribbon is formed from the constrained puddle beneath the nozzle. The enlarged view represents the heat transfer model during solidification of the ribbon. To solve Eq. [5], the following assumptions have been made:

(a) The top surface and edges of the ribbon are adiabatic.
(b) The interface between wheel and ribbon is subjected to convective heat transfer (heat transfer coefficient, h).
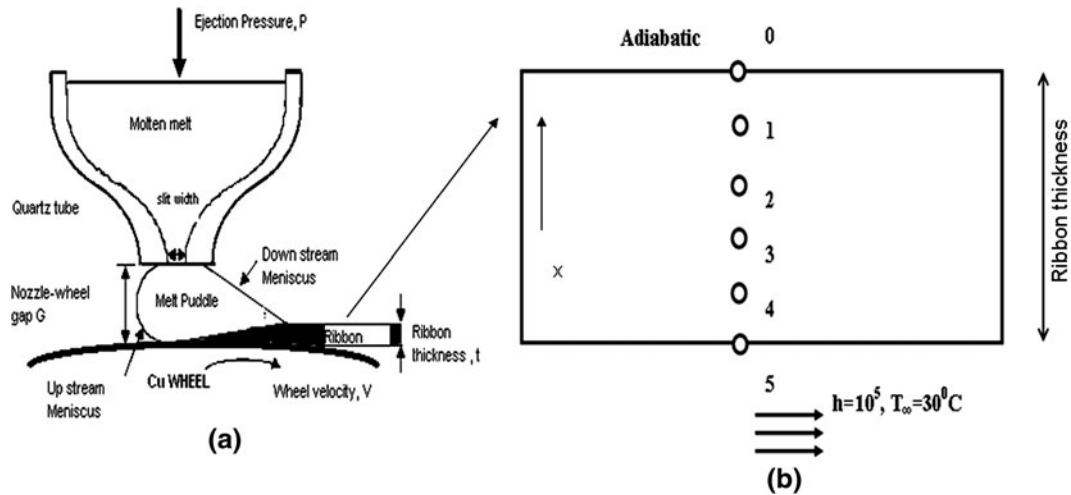
Fig. 12—Schematic representation of (a) the melt puddle in PFMS process and (b) heat transfer conditions along the thickness direction of ribbon.
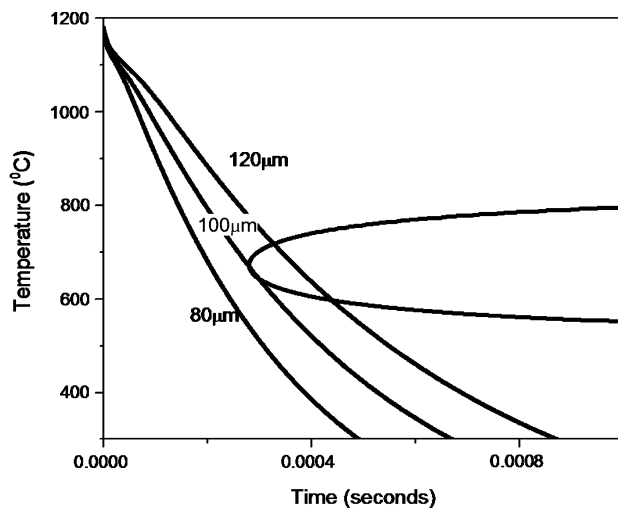

Fig. 13—Calculated cooling curves at the initial melt temperature of 1453 K (1180 °C) and TTT curve for homogenous nucleation of $Fe_{68.5}Si_{18.5}B_9Nb_3Cu_1$ alloy.

(c) The wheel is maintained at room temperature.
(d) The thermal conductivity k is same for liquid and solid alloy.

The temperatures were calculated sequentially with the time at six nodes (n) where $n = 0$ stands for the surface of the ribbon and $n = 5$ stands for the interface between wheel and the ribbon. The calculated cooling curve at the surface of the ribbon ($n = 0$) for different ribbon thickness in shown in Figure 13.

The TTT curve was calculated using the Ulhmann equation[28] where the time (t) required for homogenous nucleation of a small fraction crystallized, generally considered as 10^{-6} at a temperature (T) is given as follows:

$$t = \frac{9.3\eta}{kT}\left(\frac{a_0^9 \times 10^{-6}}{f^3 N_v}\right)^{1/4}\exp\left(\frac{1.02}{T_r^3 \Delta T_r^2}\right)^{1/4}$$
$$\times \left(1 - \exp\left(\frac{-\Delta H_f}{RT}\Delta T_r\right)\right)^{-3/4} \quad [6]$$

where η is the viscosity of the undercooled melt, $\ln \eta = 6.75 \times 10^{-5} + \frac{954.71}{T - 608.36}$ (Volger-Fulcher relation) given by Chen Dong et al.[24] a_0 is the average atomic diameter, f is the fraction of sites on the interface where atoms are added or removed $\approx 0.2\,\Delta T_r$, N_v = number of atoms per unit volume, T = temperature (K), T_r = reduced temperature = T/T_m, ΔT_r = reduced under cooling = $(T_m - T)/T_m$, and ΔH_f = molar heat of fusion.

Although the exact values of material parameters such as thermal diffusivity, heat transfer coefficient, surface tension, viscosity, density, etc. are not available for the Fe-Si-B-Nb-Cu alloy, the values have been taken from the data available in the literature for similar alloys. Table I gives the values of the parameters used for the theoretical calculations.

Figure 13 shows typical cooling curves for ribbons of different thicknesses superimposed on a TTT curve for homogeneous nucleation when the pouring temperature is 1453 K (1180 °C) (superheat temperature of 100 K (100 °C) above the melting point of alloy). It can be observed that the cooling curve for 100-μm-thick ribbon bypasses the nose of the TTT curve. Therefore, the 100-μm thickness can be considered as the critical thickness for the formation of amorphous phase while pouring from 1453 K (1180 °C). XRD patterns of as spun ribbons processed at 1523 K (1250 °C) and 17 m/s wheel speed Figure 9(a)) indicate the presence of amorphous phase in ribbons of 80-μm thickness, which is close to the calculated critical thickness.

Figure 14 shows the variation of calculated critical thickness for the formation of amorphous phase as a function of melt temperature. It is evident that the critical thickness reduces with temperature. The actual thickness vs melt temperature for ribbons produced at 17 m/s is also superimposed in the graph (Figure 14). It can be noted that the trend is similar to the Figure 7 for 34 m/s ribbons. From Figure 14 it can be observed that at a higher melt temperature, the ribbon thickness crosses the limit of the critical thickness value. This leads to the formation of crystalline phase in the as-spun ribbon when processed at a high melt temperature.

Table I. Various Parameters Used for Theoretical Calculations

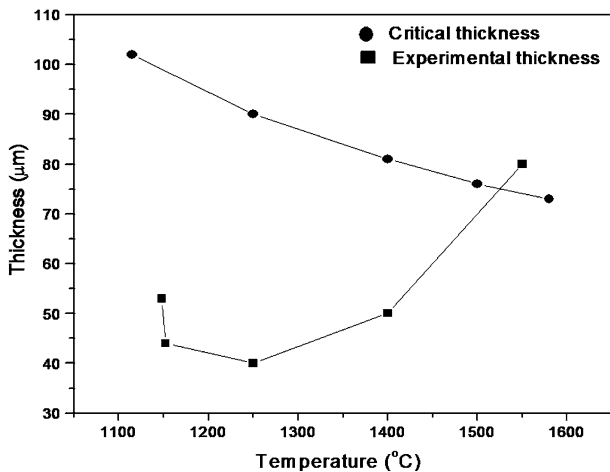| Designation	Parameters	Values	Remarks
B	constant	0.082	24
C	constant	1463.48	24
σ	surface tension	1400 mNm^{-1}	25
k	thermal conductivity	30.3 Wm^{-1}K^{-1}	29
h	heat transfer coefficient	10^5 Wm^{-2}K^{-1}	30
ρ	density	7400 kgm^{-3}	measured
a_0	average atomic diameter	3.2 Å	calculated
T_m	melting point of Fe$_{68.5}$Si$_{18.5}$B$_9$Nb$_3$Cu$_1$ alloy	1360 K (1087 °C)	measured using
ΔH_f	molar heat of fusion	13.3 kJmole^{-1}	high-temperature
C_p	specific heat at constant pressure	191 Jkg^{-1}K^{-1}	differential scanning calorimetry
T_∞	temperature of the copper wheel	303 K (30 °C)	room temperature
K	boltzmann constant	1.38×10^{-23} JK^{-1}	
N_v	number of atoms per unit volume	9.3×10^{28} m^{-3}	
g	acceleration caused by gravity	9.81 ms^{-2}	
R	gas constant	8.314 Jmol^{-1}K^{-1}	

Fig. 14—Calculated critical thickness for the formation of amorphous phase at different initial melt temperature. The experimental observed thickness is also shown.

V. CONCLUSIONS

1. During planar flow melt spinning, the stability in the puddle increases with the decrease of wheel speed, whereas high pressure results in blowing out of the downstream meniscus. A higher nozzle wheel gap enhances flow of the melt into the puddle.
2. The instability of the liquid puddle is responsible for the surface roughness either in the form of protruded striation at a lower temperature or grooves/porosity along the ribbon length at a higher temperature. Roughness also increases with wheel speed.
3. Lower ejection pressure, nozzle wheel gap, and an intermediate wheel speed, melt temperature (1523 K to 1573 K [1250 °C to 1300 °C]) favor the formation of thin and lengthy ribbons.
4. A processing map in PG/2σ (maximum operating value of pressure parameter) vs Reynolds number (Re) diagram has been established where all successful runs can be observed within a window of processing parameters.
5. The ribbons processed at a low melt temperature are completely amorphous phase, whereas dendrites of Fe$_3$Si phase embedded in amorphous matrix are found in the ribbon processed at high melt temperature. The presence of Fe$_3$Si dendrite deteriorates the soft magnetic properties.
6. The calculated critical thickness for the formation of amorphous phase is found to decrease with increasing melt superheat. The actual ribbon thickness increases with melt temperature and crosses the limit of critical thickness value leading to the formation of partially crystalline ribbons.

REFERENCES

1. M.C. Narasimhan and N.J. Flanders: US Patent 4142571, 1979.
2. R. Hasegawa: *J. Magn. Magn. Mater.*, 2000, vols. 215–216, pp. 240–45.
3. P.H. Steen and C. Karcher: *Annu. Rev. Fluid Mech.*, 1997, vol. 29, pp. 373–97.
4. L.A. Anestiev: *Mater. Sci. Eng. A*, 1991, vol. 131A, pp. 115–21.
5. H. Yu: *Metall. Trans. B*, 1988, vol. 19B, pp. 557–62.
6. M. Haddad-S and G. Amberg: *Int. J. Rapid Solidif.*, 1993, vol. 7, pp. 255–67.
7. T.J. Praisner, J.S.J. Chen, and A.A. Tseng: *Metall. Mater. Trans. B*, 1995, vol. 26B, pp. 1199–1208.
8. Z. Gong, P. Wilde, and E.F. Matthys: *Int. J. Rapid Solidif.*, 1991, vol. 6, pp. 1–28.
9. M. Bussmann, J. Mostaghimi, D.W. Kirk, and J.W. Graydon: *Int. J. Heat Mass Trans.*, 2002, vol. 45, pp. 3997–4010.
10. S.L. Wu, C.W. Chen, W.S. Hwang, and C.C. Yang: *Appl. Math. Model.*, 1992, vol. 16, pp. 394–403.
11. C.J. Byrne, E.A. Theisen, B.L. Reed, and P.L Steen: *Metall. Mater. Trans. B*, 2006, vol. 37B, pp. 445–56.

12. P.D. Wilde and E.F. Matthys: *Mater. Sci. Eng. A*, 1992, vol. 150A, pp. 237–47.
13. Y. Yoshizawa, S. Oguma, and K. Yamauchi: *J. Appl. Phys.*, 1988, vol. 64, pp. 6044–46.
14. B. Majumdar and D. Akhtar: *Bull. Mater. Sci.*, 2005, vol. 28, pp. 395–99.
15. M.E. McHenry, F. Johnson, H. Okumura, T. Ohkubo, A. Hsiao, V.R.V. Ramanan, and D.E. Laughlin: *Scripta Mater.*, 2003, vol. 48, pp. 881–87.
16. H. Okumura, M.E. McHenry, and D.E. Laughlin: *J. Magn. Magn. Mater.*, 2003, vol. 267, pp. 347–56.
17. M. Srinivas, B. Majumdar, D. Akhtar, A.P. Srivastava, and D. Srivastava: *J. Mater. Sci.*, 2011, vol. 46, pp. 616–22.
18. Y. Yoshizawa, K. Yamauchi, and S. Oguma: European Patent 0271657, 1988.
19. A.K. Panda, S. Roy, S.R. Singh, V. Rao, S. Pramanik, I. Chattoraj, A. Mitra, and P. Ramchandrarao: *Mater. Sci. Eng. A*, 2001, vol. 304 (6A), pp. 457–61.
20. V.I. Tkatch, A.I. Limanovskii, S.N. Denisenko, and S.G. Rassolov: *Mater. Sci. Eng. A*, 2002, vol. A323, pp. 91–96.
21. E.P. Barth, F. Spaepen, R.L. Bye, and S.K. Das: *Acta Mater.*, 1997, vol. 45, pp. 423–28.
22. J.K. Carpenter and P.H. Steen: *J. Mater. Sci.*, 1992, vol. 27, pp. 215–25.
23. F.A. Nichols and W.W. Mullims: *Trans. TMS-AIME*, 1965, vol. 233, pp. 1840–48.
24. L.I. Chen Dong, T. Xue Lei, C. Xi-Chen, and A.G. Ilinsky: *Chin. Phys. Lett.*, 2003, vol. 20, pp. 395–97.
25. M. Tomut and H. Chiriac: *Mater. Sci. Eng. A*, 2001, vol. A304 (6), pp. 272–76.
26. R. Alben and J.J. Becker: *J. Appl. Phys.*, 1978, vol. 49, pp. 1653–58.
27. F.P. Inropera and D.P. Dewitt: *Fundamentals of Heat and Mass Transfer*, Wiley, New York, NY, 1985.
28. H.A. Davies, J. Aucote, and J.B. Hull: *Scripta Metall.*, 1974, vol. 8, pp. 1179–90.
29. V.I. Tkatch, S.N. Denisenko, and B.I. Selyakov: *Acta. Metall. Mater.*, 1995, vol. 43, pp. 2485–91.
30. V.I. Tkatch, S.N. Denisenko, and O.N. Beloshov: *Acta. Mater.*, 1997, vol. 45, pp. 2821–26.